

# Giant elastic-wave asymmetry in a linear passive circulator

Received: 7 August 2024

Accepted: 17 April 2025

Published online: 29 April 2025

 Check for updatesYabin Hu<sup>1,2</sup>, Yongbo Li<sup>1</sup>, Yongquan Liu<sup>3</sup>✉, Bing Li<sup>1,4</sup>✉ & Johan Christensen<sup>2</sup>✉

Nonreciprocal transmission of waves is highly desirable for the transport and redistribution of energy. However, building an asymmetric system to break time-reversal symmetry is relatively difficult because it tends to work under stringent guidelines, narrow bandwidth, or external impetus, particularly in a three-port system. Without breaking reciprocity, realizing “one-way” transmission of elastic waves by a linear and passive structure in a higher-dimensional asymmetric system, such as a three-port circulator, poses quite a challenge. Here, based on the wave-vector modulation mechanism, we propose an elastic-wave circulator that achieves this without breaking reciprocity, enabling perfect mode transition and wave trapping simultaneously. Requiring neither activated media nor relying on the nonlinearity of nonreciprocal devices, the circulator routes elastic waves purely in a clockwise direction, offering superior performance in broad bandwidth, robust behavior, and simple configuration. Our study provides a feasible platform for asymmetric wave transport in a three-port system, which can be useful in the routing, isolation, and harvesting of energy and can also be extended to other fields, such as electromagnetic and acoustic waves.

The pursuit of a nonreciprocal system, characterized by entirely distinct received-transmitted field ratios upon swapping the source and detector, holds profound significance in both fundamental research and applied science<sup>1–5</sup>. Central to achieving nonreciprocity lies in breaking the time-reversal symmetry, primarily accomplished through the utilization of nonlinear media<sup>6–10</sup> or active elements<sup>11–15</sup>. Despite their effectiveness, these approaches are universally constrained by limitations including signal distortion<sup>6,7,16</sup>, amplitude degradation<sup>17,18</sup>, and system intricacy<sup>19</sup>.

Notably, all linear and time-invariant systems inherently exhibit reciprocity unless external fields are applied to introduce biased motion, thus breaking time-reversal symmetry<sup>20–23</sup>. A pioneering research<sup>20</sup>, analogous to the Zeeman effect<sup>24</sup>, has realized an acoustic circulator by implementing an angular momentum bias induced by a circulating fluid, facilitating only unidirectional clockwise or

anticlockwise wave propagation. However, this active nonreciprocal Zeeman circulator relies on precise alignment between the resonant frequency and additional momentum source, resulting in limitations of low tolerance, sophisticated settings, and narrow bandwidth.

On the other hand, the principle of reciprocity proves stubbornly persistent and challenging to circumvent. In nature where the medium is passive and linear, reciprocity is almost assured. Consequently, intriguing and useful asymmetric wave phenomena have been exploited in reciprocal frameworks to facilitate one-way propagation, akin to nonreciprocal energy flux. Noteworthy advancements have been made in creating asymmetric wave phenomena through linear, passive artificial structures, such as spatially asymmetric waveguides<sup>25–27</sup>, topological insulators<sup>28–30</sup>, asymmetric high-order diffractions<sup>31–34</sup>, and systems demonstrating strong asymmetry at exceptional points<sup>35–37</sup>. These paradigms can be considered as effective

<sup>1</sup>School of Aeronautics, Northwestern Polytechnical University, Xi'an, Shaanxi 710072, China. <sup>2</sup>IMDEA Materials Institute, Calle Eric Kandel, 2, 28906 Getafe, Madrid, Spain. <sup>3</sup>State Key Laboratory for Strength and Vibration of Mechanical Structure, School of Aerospace Engineering, Xi'an Jiaotong University, Xi'an 710049, China. <sup>4</sup>National Key Laboratory of Strength and Structural Integrity, Xi'an 710072, China. ✉e-mail: [liuy2018@xjtu.edu.cn](mailto:liuy2018@xjtu.edu.cn); [bingli@nwpu.edu.cn](mailto:bingli@nwpu.edu.cn); [johan.christensen@imdea.org](mailto:johan.christensen@imdea.org)

platforms for asymmetric wave transmission in one direction yet blocking in the opposite direction for a two-port system.

Specifically, in elastodynamics, elastic waves exhibit richer polarizations and dispersion characteristics absent in other fields. In addition, the coupling or conversion between different polarized modes significantly amplifies the complexity of the system, presenting an extra hurdle as a result. On the other hand, achieving the asymmetric behavior in elastic fields brings fascinating consequences and unique properties. Many pioneering works on the asymmetric transport of elastic waves have been reported. By unveiling the intrinsic spin, the strong asymmetric excitation of a spin-selected elastic wave can be realized based on the spin–momentum locking<sup>38</sup>. Willis coupling is another approach to break the symmetry in elastic solid, enabling asymmetric reflection of flexural waves<sup>39</sup>. Intrinsic asymmetry of the unit cell can also be harnessed to achieve asymmetric negative refraction<sup>40</sup>, as well as asymmetric topological edge modes<sup>41</sup>. In addition, the inevitable material dissipation can be taken advantage to create the unidirectional flexural wave absorption at the exceptional point<sup>36</sup>. However, extending these linear passive strategies to a higher-dimensional asymmetric system such as a three-port circulator<sup>42,43</sup>, presents significant challenges because such asymmetric structures cannot keep the uniformity of each port. It seems to be a challenging problem to overcome the fundamental bounds determined by the Lorentz reciprocity theorem and the physics laws<sup>44</sup>. To build a circulator with same-configuration ports, a biased field which breaks the reciprocity has to be introduced, yet led to a sophisticated system as a result. The acoustic nonreciprocal circulator has already uncovered the dilemma, as well as the recent proposed photon<sup>45</sup> and heating circulator<sup>43</sup>. Some promising methods have been demonstrated in ring cavities coupling with emitters or engineered dissipation, which are endowed with chiral reversal and unidirectional radiation at exceptional point<sup>46–48</sup>. Taking into account delicate balancing to acquire non-Hermitian degeneracy at exceptional point, a broadband and robust elastic circulator without breaking time-reversal symmetry demands inevitably new strategy to develop.

This article introduces a generic framework to orchestrate exclusively clockwise routing of elastic waves using a compact, higher-dimensional circulator in a linear passive setting. Borrowing concepts from the acoustic Zeeman effect, wave-vector splitting is ingeniously employed to obtain strong asymmetry without relying on nonlinearity or active modulation. Through precise tailoring of the wave-vector, a waveguide with identical profiles at both ends is designed, facilitating perfect mode transition and total wave trapping across opposite inputs. Integrating three such waveguides with rotation symmetry can form a circulator by coupling them end-to-end. Neither relying on spatial-temporal modulation of an active medium, nor requiring material nonlinearity to generate nonreciprocal behavior, our linear passive circulator demonstrates substantial asymmetric wave directionality for each port input. Unlike angular momentum-biased circulator dependent on fluid velocity or material nonlinearity, the paradigm we propose offers notable superiorities with simple configuration, broad bandwidth and robust performance which can also be extended to other wave physics like electromagnetic and acoustic analogs.

## Results

### Linear passive circulator

Our paradigm revisits the concept established by the acoustic Zeeman circulator<sup>20</sup>, renowned for its remarkable nonreciprocity. As illustrated in Fig. 1a, the acoustic circulator utilizes a circulating fluid that facilitates a frequency shift of  $\Delta\omega$ , leading to the resonant frequency splitting between right- and left-handed modes. Mirroring the electronic Zeeman effect, an incoming sound at port I is unevenly split into two distinct frequency branches,  $\omega_0 \rightarrow \omega_+$  and  $\omega_0 \rightarrow \omega_-$ , respectively. The operational parameters, such as the speed of the circulating

air, are calibrated based on the total quality factor (Q-factor) of the dipolar resonance, transforming the system into a highly efficient acoustic nonreciprocal circulator. Notably, the specific velocity of the circulating fluid emerges as a crucial factor for breaking the system reciprocity, while total transmission and blocking at port II and III are subject to precise conditions of rigorous frequency  $\omega_0$  and cavity radius, pointing to the stringent nature of this design. The limitations inherent in the above scheme have propelled us to explore new strategies for realizing an effective acoustic or elastic circulator without external disturbances, active modulation, or nonlinearity.

In this pursuit, we first devised a novel method to achieve one-way elastic circulator purely through linear and passive media, focusing on the splitting of wave vector rather than angular frequency. Illustrated in Fig. 1b, our design features three identical curved waveguides with chiral symmetric arrangement at  $120^\circ$  intervals. Specifically examining incident waves from port I, the circular wave vector component,  $k_\theta$ , is engineered to increase gradually along the clockwise direction. Consequently, at port II,  $k_\theta$  will transition to  $k_+$  ( $k_+ = k_0 + \Delta k > 0$ ), thereby facilitating smooth propagation of incoming waves into port II. Conversely, to hinder wave propagation along the counter-clockwise direction, the circular wave vector component  $k_\theta$  at port I should be diminished to zero before reaching port III. Owing to the symmetry of the three interlinked waveguides, the linear and passive system will only support one-way energy flowing, specifically in a clockwise sequence from port I to II, II to III, and III back to I.

To illustrate the tailoring physics, we present the variation of circular wave vector component,  $k_\theta$ , with varying waveguide mediums, as shown in Fig. 1c. Specifically,  $k_\theta$  is expected to incrementally ascend from  $k_0$  to  $k_+$  between port I and II, depicted by the formula  $k_+ = k_0 + \Delta k$ . To achieve this envisioned scenario, a smooth alteration in the medium's effective properties is necessary. Nonetheless, the circulators at ports I, II, and III possess identical physical properties, achieving asymmetric transmission necessitates an intentional disruption of the waveguide's spatial symmetry. This deliberate disruption inevitably introduces an interface characterized by a sudden shift in the effective properties. The abrupt interface not only requires break the spatial symmetry, but also ensures the continuity of wave vector. Concurrently, the resonant modes within the waveguide will be compelled to a transition from one mode (represented on the  $x$ -axis in red) to another (represented on the  $x$ -axis in blue) at this strategically placed interface. Therefore, the critical challenge for smooth propagation from port I to port II lies in the seamless realization of a perfect mode transition at the abrupt interface.

On the contrary, to block wave propagation along the anticlockwise direction, the wave vector  $k_\theta$  at port I should decrease and reach zero prior to port III. The zero wave vector implies that the waves will be trapped here and incapable of propagating forward. Mathematically,  $k_\theta$  at port III has a negative value  $k_-$ , where  $k_- = k_0 - \Delta k$ . However, we want to emphasize that the negative wave vector  $k_-$  ( $x$  axis in dashed line) is not actually obtained in practice because of the terminate of wave propagation at zero wave vector location. Therefore, the second key point for wave trapping before port III is tailoring the wave vector  $k_\theta$  from  $k_0$  to zero in continuous waveguide medium. By doing so, without breaking the reciprocity of system, we obtain nonsymmetrical scattering matrix,

$$S = \begin{bmatrix} 0 & 1 & 0 \\ 0 & 0 & 1 \\ 1 & 0 & 0 \end{bmatrix} \quad (1)$$

### Realization of elastic-wave circulator via wave-vector modulation

Achieving perfect mode transition and suppression, simultaneously, along the opposite directions in an identical waveguide

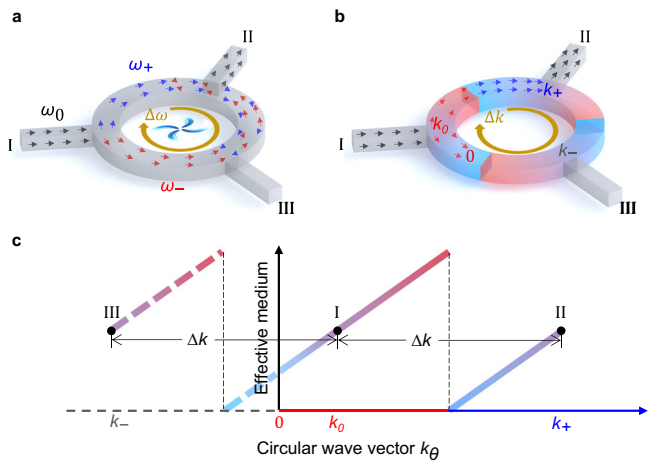


**Fig. 1 | Illustration of elastic-wave circulator based on wave-vector modulation.** **a** Nonreciprocal acoustic circulator by implementing biased angular momentum. The inputting angular frequency  $\omega_0$  is split into  $\omega_+$  and  $\omega_-$  by circulating field,  $\omega_\pm = \omega_0 \pm \Delta\omega$ . **b** Elastic-wave circulator by tailoring wave vector. The inputting circular wave vector  $k_0$  is modulated into  $k_+$  and  $k_-$ ,  $k_\pm = k_0 \pm \Delta k$ . Here,  $k_+ > 0, k_- < 0$ . **c** Schematic of elastic-wave circulator based on wave vector modulation. The gradient color of the line indicates the variation of circular wave vector  $k_\theta$  with different arrangements of effective medium. The mode transition is represented by the red and blue axis. Port I, port II and port III have the same effective medium.

is the key factor to design the linear passive elastic circulator. Figure 2a shows the circulator with varying unit cells along the waveguide edges. The unit cell is marked A at the three ports I, II, III. The abrupt interface featuring substantial dissimilarity of unit cells ( $B_1$  and  $B_2$ ) at two sides exists which is denoted by yellow dashed line. Another unit cell is marked C where mode suppression occurs and elastic waves are reflected back. The frequency spectrum of flexural modes for a unit cell is calculated and shown in Fig. 2b. The length, thickness, width of unit cell are  $H=10$  mm,  $\tau=1.5$  mm,  $\delta=20$  mm, respectively. Two same cantilever beams are connected on both sides, with a width of  $h=5$  mm. For a specific cantilever beam with the length  $l$ , the frequency spectrum profiles of unit cells can be calculated theoretically. A waveguide composed of the periodic arrangement of unit cells supports guided modes in the following form,

$$w_1 = \begin{cases} [P \cos h(\xi_1 y) + Q \cos h(\xi_2 y)] e^{-ik_x x} & \text{(mode 1)} \\ [P \cos(\xi_1 y) + Q \cos h(\xi_2 y)] e^{-ik_x x} & \text{(mode 2)} \end{cases} \quad (2)$$

wherein for mode 1,  $\xi_1 = \sqrt{k_x^2 - k^2}$  and  $\xi_2 = \sqrt{k^2 + k_x^2}$ . For mode 2,  $\xi_1 = \sqrt{k^2 - k_x^2}$  and  $\xi_2 = \sqrt{k^2 + k_x^2}$ . Since the width of cantilever beam is much smaller than the operating wavelength, we can only consider the fundamental mode in the cantilever beam,

$$w_2 = a e^{-jky} + b e^{jky} + c e^{-ky} + d e^{ky} \quad (3)$$

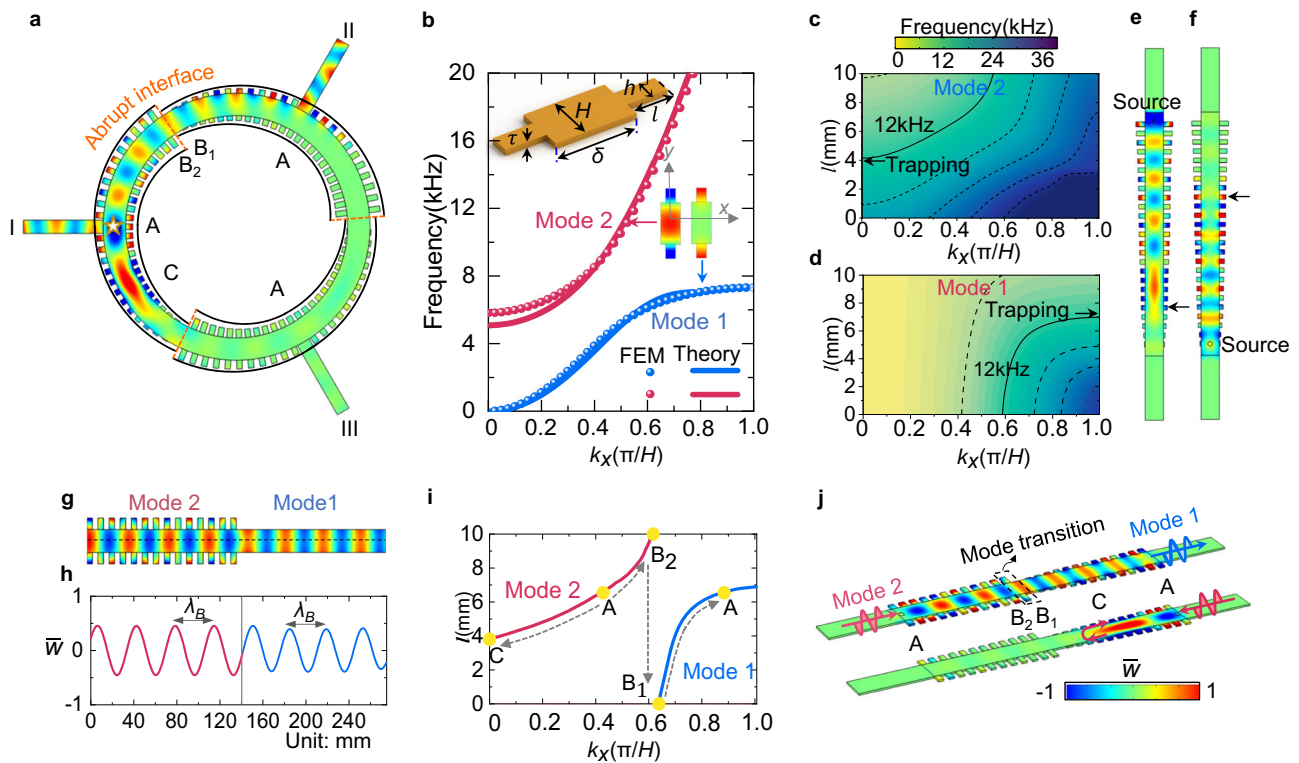


**Fig. 2 | The mechanism of elastic-wave circulator.** **a** The circulator model and one-way wave behavior. Several locations (A,  $B_1$ ,  $B_2$ , C) are selected to analyze the evolution of wave vector. **b** The frequency spectrum of flexural waves. The unit cell configuration and the eigenmodes of mode 1 and mode 2 are provided as the insets.  $H=10$  mm,  $h=5$  mm,  $\delta=20$  mm,  $\tau=1.5$  mm.  $l$  is the cantilever beam length in the unit cell. **c, d** The frequency spectrum contour of mode 2 and mode 1 with different unit cells. **e, f** Wave trapping of mode 2 and mode 1 at 12 kHz. The trapping locations

are marked by black arrows, which correspond to that in (c, d). **g** Nearly perfect mode transition at the abrupt interface. **h** Normalized out-of-plane displacement  $\bar{w}$  along the middle line of waveguide in (g).  $\lambda_B$  represents the wave length of mode 2 and mode 1. **i** The evolution of wave vector  $k_x$  with different unit cells at 12 kHz. **j** Simulated displacement fields  $\bar{w}$  in one-way waveguide, which has same unit cells at two ports. The abrupt interface in the middle allows mode transition and suppression for the left and right incident, respectively.

Considering the free boundary condition at the end of cantilever beam and applying the continuity conditions of displacement, slope, bending moment, shear force at the interface between cantilever beam and waveguide channel, we can derive the following relation (see Supplementary Note1 and Supplementary Fig. S1 for details).

$$\mathbf{T} \cdot [PQabcd]^T = \mathbf{0} \quad (4)$$

Given the cantilever beam  $l = 10$  mm as an example, the analytical dispersion bands (Theory) are derived by solving  $\det(\mathbf{T}) = 0$ , and agree well with numerical solutions (FEM), as compared in Fig. 2b. The eigenstates of two modes are provided, in which mode 1 ( $k_x > k$ ) and mode 2 ( $k_x < k$ ) exhibit the hallmark traits of surface waves and propagating waves, respectively. We numerically calculated the dispersion bands when the length of cantilever beam ranges from 0 mm to 10 mm. The dispersion spectrum contours for mode 2 and mode 1 are depicted in Fig. 2c, d, respectively. The equifrequency line gives the relations between wave vector  $k_x$  and cantilever beam length  $l$ . We take the equifrequency line at 12 kHz (black solid line) for the following discussion. The wavevector  $k_x$  can be smoothly tailored by increasing or decreasing  $l$  until reaching the Brillouin zone boundary 0 or  $\pi/H$ . Specifically, if the waveguide is built with varying cantilever beam length  $l$ , the wave vector  $k_x$  of mode 2 can be decreased to 0 at the location  $l = 4.1$  mm, which implies wave trapping of mode 2. The corresponding numerical result is shown in Fig. 2e. The similar phenomenon can also be found for mode 1. With the increase of cantilever beam length  $l$ , the wave vector  $k_x$  will reach  $\pi/H$  at the location  $l = 7.1$  mm. The simulated wave trapping of mode 1 can be observed in Fig. 2f. One of key factors for the unidirectional circulator, wave trapping, can be achieved based on the above strategy.

Besides wave trapping, another key factor is to realize perfect mode transition between surface mode (mode 1) and propagation mode (mode 2). For this pursuit, we utilize wave vector  $k_x$  of two modes to establish the matching impedance. We deduced that the impedance  $Z$  of waveguide along the wave propagating direction as

$$Z = iD \left[ \frac{k^2 \nu}{k_x} + k_x(1 - \nu) \right] \quad (5)$$

where  $D, k, \nu$  are bending stiffness, wave number, Poisson's ratio of host plate, respectively.  $k_x$  is the wave vector along the wave propagating direction  $x$  (see Supplementary Note 2, Supplementary Fig. S2 and Fig. S3 for detailed derivation). The impedance  $Z$  only depends on the wave vector  $k_x$  if the waveguide channel keeps constant, which means perfect mode transition can be generated if the two modes possess the identical wave vector  $k_x$ . From the dispersion spectrum contours, we notice that mode 2 and mode 1 have the same wave vector  $k_x$  when  $l = 10$  mm and  $l = 0$  mm at 12 kHz, which illustrates that impedance matching condition can be satisfied at the abrupt interface between two entirely dissimilar unit cells. To demonstrate this point, we deployed the full wave simulation to display wave propagation around the abrupt interface. Figure 2g exhibits that mode 2 and mode 1 can be transferred smoothly at the abrupt interface with a slight backscattering. The transmission coefficients between different unit cells are calculated and provided in Supplementary Note 3 and Fig. S4. The normalized out-of-plane displacement  $\bar{w}$  along the middle line of the waveguide (black dashed line) is shown in Fig. 2h. We can clearly observe that the amplitude and wavelength almost remain unchanged at both sides of the abrupt interface.

The nearly perfect mode transition facilitates smooth wave propagation at the abrupt interface. In light of this principle, we propose a framework for one-way waveguide with identical end ports. It incorporates two gradient waveguides connected by an abrupt interface, as detailed in Fig. 2j. Both the left and right ports have the same unit cell A and the bilateral unit cells of abrupt interface are marked by B<sub>2</sub> and B<sub>1</sub>.

When the flexural waves inputs from the left to the right, they will experience the path A → B<sub>2</sub> → B<sub>1</sub> → C → A. Figure 2i exhibits the evolution of wave vector  $k_x$  with the changing of unit cells. The flexural waves mostly coupled into mode 2 at the location A will arrive at the left side of interface, where mode 2 at B<sub>2</sub> is converted into mode 1 at B<sub>1</sub>. Here, we place the source on the middle line of the ring near port I, which is essential to ensure that mode 2 is dominantly coupled. If the source is placed in the port, the flexural waves will not couple into mode 2, and a pure asymmetric transmission cannot be guaranteed. The reasons behind it are fully discussed in Supplementary Note 4, Fig. S5, and Fig. S6. After that, flexural waves of mode 1 will be delivered into the right port. During the whole process, wave vector  $k_x$  keeps increasing evenly which ensures the highly efficient transmission from the left to right. Conversely, when the flexural waves input from the right to the left, they will be trapped at location C. The intrinsic mechanism can also be exploited by analyzing the changes of wave vector  $k_x$  in Fig. 2i. During the path A → C, the wave vector  $k_x$  of mode 2 will undergo sustainable decrease until reaching zero at location C. Mode transition is unlikely to happen here because no same wave vector can be found at the mode 1 branch. As a result, flexural waves in mode 2 will be reflected at location C. The above statements are validated by numerical simulation in Fig. 2j, demonstrating that the proposed waveguide with same ports allows flexural waves propagating from the left smoothly but almost totally blocked from the right.

Based on this prototype, we constructed an engineered circulator with three interconnected waveguides (Fig. 2a). Here we place the excitation source at port I (marked by a white star) and the full-wave simulation of normalized out-of-plane displacement is exhibited at 12 kHz. Along the clockwise direction, the flexural waves coupled into mode 2 at port I, enable seamless propagation into the abrupt interface. After passing through the interface, mode 2 is converted into mode 1 and continue propagating into the port II. Conversely, waves along the anticlockwise direction can be only trapped into location C prior to the interface and bounced back, preventing energy flux from reaching port III. To the end, the robust effectiveness of this linear passive circulator with three-fold rotation symmetry is demonstrated in filtering and directing wave propagation as designed. The transient responses in time domain are provided in Supplementary Movie 1.

## Experimental realization

To verify the one-way propagation in the designed elastic-wave circulator, we built the experimental setup as illustrated in Fig. 3a. The circulator is fabricated through wire electrical-discharge machining on a steel plate with a thickness of 1.5 mm. The diameter of circulator is 200 mm and the waveguide channel has a width of 20 mm. The inset shows an enlarged view of the abrupt interface. We conducted a series of experimental verifications by placing the point source near port I, port II and port III, respectively. The experimental results at 11.2 kHz are exhibited in Fig. 3b. When the source is placed near port I, the flexural waves energy can only flow clockwise from port I into port II but not port III. Similar one-way propagation phenomena are also captured for other source locations. Because of the rotational symmetry of circulator, the displacement fields should remain identical regardless of which port the source is placed at. However, some discrepancies can be observed especially within the input and output channels, which may be induced by manufacturing and measurement errors. To clarify this, the corresponding numerical simulations and discussions are provided in the Supplementary Note 5 and Fig. S7.

In each panel of Fig. 3b, the normalized maximum amplitudes  $|\bar{w}|_{\max}$  varying with the azimuth in the waveguide channel are shown inside the circulator. With the sustainable increase of wave vector  $k_x$ , energy gradually accumulates at waveguide edge along the clockwise direction. Conversely, the decrease of wave vector  $k_x$  along the counterclockwise direction results in the stopping of flexural waves, where the peak value of  $|\bar{w}|_{\max}$  appears and no energy flowing beyond

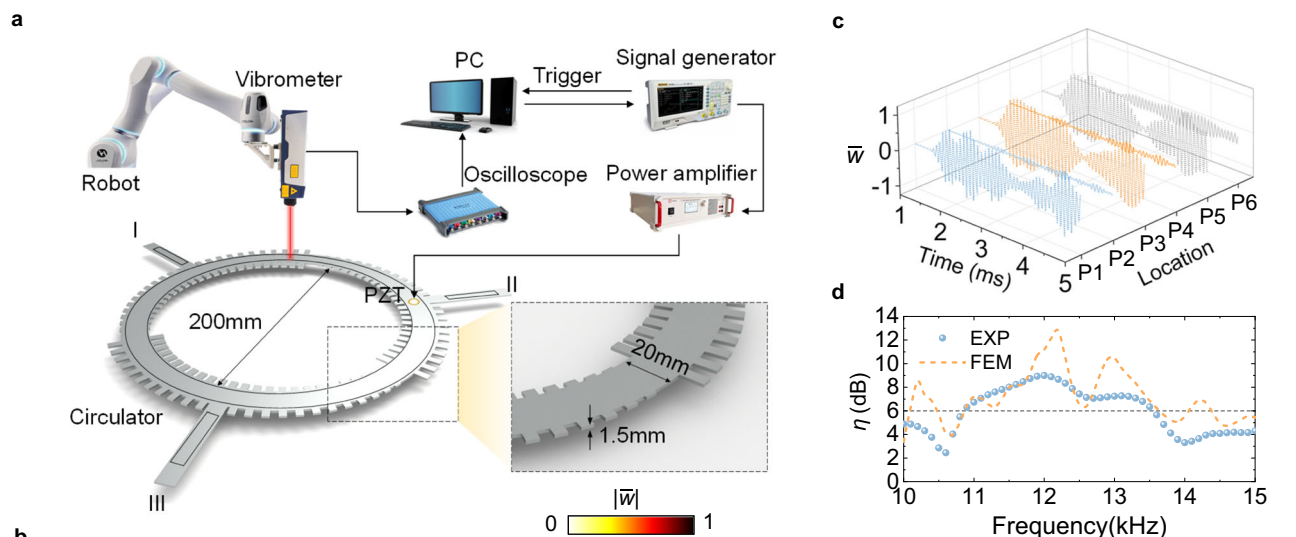


**Fig. 3 | The experimental demonstration of elastic-wave circulator.** **a** The setup of experimental platform. **b** The experimentally measured normalized out-of-plane amplitude  $|\bar{w}|$  at 11.2 kHz when the source is placed near port I, port II and port III, respectively. The black solid lines in the circulators represent the maximum of  $|\bar{w}|$  at different azimuths, and the red box regions are selected for the calculation of contrast ratio  $\eta$ . **c** The measured normalized out-of-plane displacement  $\bar{w}$  in time

domain. P1–P6 are selected in the centers of six ports in **(b)**. The blue, orange and gray lines correspond to the inputting near port I, port II and port III, respectively. **d** Numerically simulated (FEM) and experimentally measured (EXP) contrast ratio  $\eta$  as the function of frequency. The baseline of extremely high asymmetry is  $\eta = 6$ , above which highly asymmetry can be obtained from 11 to 13.5 kHz.

this point. In each panel of Fig. 3b, we select two points (marked by blue stars) at the centers of outputting ports to analyze the displacement variations in time domain. As shown in Fig. 3c, the measured oscillating normalized out-of-plane displacement  $\bar{w}$  at clockwise outputting is significantly larger than that at anticlockwise outputting wherever the inputting is.

A contrast ratio is defined to quantitatively evaluate the circulator's efficiency, which is denoted by  $\eta = 10 \log \frac{\iint_{\text{II}} |\bar{w}| dS}{\iint_{\text{III}} |\bar{w}| dS} = 10 \log \frac{\sum_{i=1}^N |\bar{w}_{\text{II}}|}{\sum_{i=1}^N |\bar{w}_{\text{III}}|}$ . Here, two same-size regions (indicated by red boxes in Fig. 3b) are selected for the integration and  $N$  is the number of sampling points. The contrast ratio  $\eta$  ensures a reliable index to quantify the asymmetry when we sum up all the sampling points in the two regions. The numerical and experimental results are shown in Fig. 3d, in which  $\eta > 2$  can be observed from 10 kHz to 15 kHz, with an extremely high contrast ratio  $\eta > 6$  maintained within the range of 11 kHz to 13.5 kHz. The numerically simulated peak value ( $\eta = 12.8$ ) is larger than the experimentally measured value ( $\eta = 9.0$ ), which could be induced by manufacturing errors and material dissipation. The scattering characteristics of circulator from different inputting are provided in Supplementary Note 6 and Fig. S8. Although flexural waves can be mostly coupled to mode 2 when the source is placed in the ring, a few waves in other modes can also be generated, which will undermine the asymmetry effect to some extent. On the other side, the dominant flexural waves in mode 2 will experience the mode transition at the abrupt interface. In fact, the transmission rate cannot reach 100% perfectly, and not all the waves can be directed into port II. All these

factors fundamentally limit the highest asymmetry efficiency  $\eta$  for the circulator. In short, the proposed passive elastic circulator demonstrates excellent asymmetry performance across a broad bandwidth. The experimental results confirm that the linear passive circulator, achieved by tailoring wave vectors  $k_x$ , allows flexural waves propagating only along the clockwise direction without relying on any external biased field or nonlinear media. Additional experimentally measured and numerically simulated normalized displacement fields  $\bar{w}$  at other frequencies and the transient responses are compared in the Supplementary Fig. S9 and Supplementary Movie 2.

### Unidirectional demultiplexing routing

Perfect mode transition and wave trapping are crucial for one-way transmission of flexural waves through the proposed wave-vector-based circulator. By addressing these pivotal issues, a gradient waveguide with discrete unit cells can be engineered into a varying-section beam, acting as a simplified version of the circulator. Intriguingly, the meticulously designed elastic circulator can further overcome the constraint of source location limited in the channel, allowing flexural waves from any port to route along the clockwise direction. As depicted in Fig. 4a, we position excitation sources at both ends of the waveguide, where no cantilever beams are attached laterally. The waveguide channel width is 30 mm. On the left side of the abrupt interface, the cantilever beam length increases from  $l = 0$  mm to  $l = 10$  mm gradually. For the right side, the beam width increases linearly from  $\delta = 22$  mm to  $\delta = 30$  mm. The full-wave simulation of

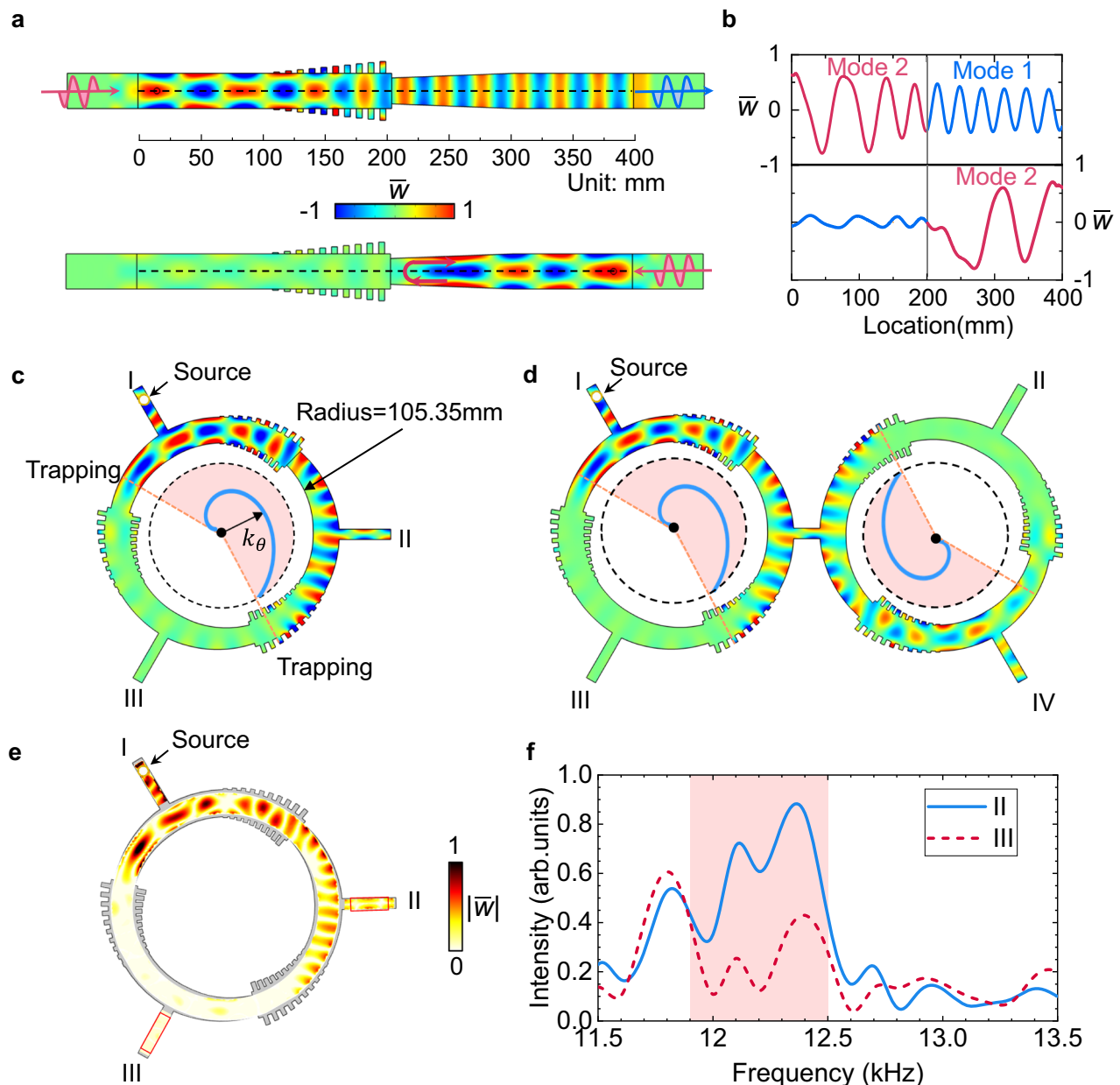


**Fig. 4 | The improved design of elastic-wave circulator. a** The simulated out-of-plane displacement field  $\bar{w}$  for the simplified waveguide at 12.4 kHz. **b** The distribution of normalized out-of-plane displacement  $\bar{w}$  along the black dashed line in (a). **c** The simulated result of improved elastic-wave circulator when the source is placed in port I. The blue curved line inside the shaded region represents the circular wave vector  $k_\theta$  from 0 to the maximum. The inner radius of circulator is

105.35 mm. **d** A double elastic-wave circulators for unidirectional demultiplexing routing. **e** The experimentally measured normalized amplitude fields  $|\bar{w}|$  at 12.4 kHz. **f** The amplitude intensity of port II and port III as a function of frequency. The intensity is obtained by integrating the amplitude in the two red boxes of e. The shaded region represents significant asymmetry between two ports.

normalized displacement field  $\bar{w}$  at 12.4 kHz is shown in the upper panel of Fig. 4a. The same asymmetric rectifying functionality as Fig. 2j is achieved by a more compact topology design.

The corresponding normalized out-of-plane displacement  $\bar{w}$  along the central line of waveguide (black dashed line in Fig. 4a) is presented in Fig. 4b. For the incident waves from the left, the displacement amplitudes remain almost constant at both sides of interface, with a progressively increasing wave vector indicated by the decreasing wavelength. Conversely, incident waves from the right side are trapped before reaching the abrupt interface. The left-side flexural waves' amplitude nearly vanishes compared to the right side, illustrating the absence of mode transition in this scenario.

We further utilize the simplified waveguides to build the single and demultiplexing elastic circulators, as illustrated in Fig. 4c, d, respectively. The simulated normalized out-of-plane displacement  $\bar{w}$  in the three-port circulator at 12.4 kHz is shown in Fig. 4c. Regardless of the excitation source's placement, only clockwise propagating of flexural waves is allowed, demonstrating the complete realization of a mechanical circulator for asymmetrically routing flexural waves without relying on nonlinear material or unbiased field perturbations. The good performance of the improved circulator is also demonstrated by experimental measurement. We provide the experimentally measured displacement amplitude fields  $|\bar{w}|$  at 12.4 kHz in Fig. 4e, which show good agreement with the simulated results (Fig. 4c). The asymmetry

intensity from 11.5 kHz to 13.5 kHz is evaluated by integrating the amplitude over port II and port III (Fig. 4f). Within the range of 11.9 kHz to 12.5 kHz, most of the energy from the source can arrive at port II with high asymmetry, demonstrating that a perfect elastic circulator can be achieved based on the modified design strategy.

Furthermore, we would like to elucidate the fact that flexural waves from port I will merely reach port II but not proceed to port III, which can be explained by wave trapping of mode 1. As the wave vector  $k_\theta$  increases from port I to port II, flexural waves are converted into surface waves. If they continue propagating along the clockwise direction,  $k_\theta$  reaches its maximum value  $\pi/H$  before the abrupt interface, causing the surface waves to be trapped and reflected (Fig. 4c). The blue Archimedes spiral inside the circulator exhibits the variation of wave vector, in which the shaded region indicates the energy transportation of flexural waves. Mode 2 and mode 1 are trapped at opposite ends of the spiral.

We extended the single circulator concept to design a double circulator prototype for unidirectional demultiplexing routing. As illustrated in Fig. 4d, one circulator connects bidirectionally to a mirror-symmetric counterpart. Consequently, energy flux from the source cannot enter ports II and III due to their equivalent placement. Between ports I and IV, the symmetric waveguide profile, with wave vector increasing firstly and then decreasing to its initial value (shaded region in Fig. 4d), ensures smooth, asymmetric flexural wave propagation from port I to port IV.

## Discussion

On the basis of the wave vector tailoring strategy, a customized circulator framework can be further realized. Taking a four-port circulator as an example, the output port can be tailored according to the customizable arrangement, enabling imparted superior versatility to this framework. As shown in Fig. 5a, a four-port circulator with mirror symmetry about port 1 and 3 enables trapping inputting waves around port 1, without any energy flowing to other ports along the circulator. The blue dashed line represents the symmetry axis. In Fig. 5b, another four-port circulator with 4-fold rotation symmetry allows flexural waves to propagate from port 1 to port 2 exclusively. In addition, the flexural wave energy flux can be continuously guided forward along the clockwise direction with different type of circulators, as shown in Fig. 5c–e. Without introducing additional devices or new physical mechanisms, we can ingeniously achieve customized energy delivery from port 1 to port 2, port 3, port 4, port 1 gradually only relying on the symmetry rules. The corresponding arranging patterns for each four-port circulator are displayed as insets of Fig. 5a–e, respectively.

Besides, the wave-vector tailoring tactics can also facilitate us to design the compact isolator only using a couple of unit cells. Here, three unit cells with a symmetrical distribution are chosen to build the isolator (as illustrated in Fig. 5f), whose lengths of cantilever beam are 4.1 mm, 6.3 mm, 10 mm, respectively. The incoming waves from one side can be reflected by the isolator owing to mismatched impedance, which behaves like the hard wall to flexural waves. Also, if the source is placed in the isolator, the vibration can be confined inside, with no energy leaking. In Fig. 5f, we displayed the normalized out-of-plane displacement fields  $\bar{w}$  at 12 kHz for the two cases and the corresponding normalized amplitudes  $|\bar{w}|$  along the middle line (black dashed line) are also plotted. To verify the broadband effectiveness of the compact isolator, the normalized amplitude  $|\bar{w}|$  versus location and frequency is illustrated in Fig. 5g, h, respectively. We can see that the peak amplitude is confined at the left half part ( $0 \sim 120$  mm) and a narrow range (80 mm  $\sim$  120 mm) from 10 kHz to 15 kHz, which corresponds to external and internal excitations, respectively. The compact isolators can also be used to map out the wave propagating route as we expect. As shown in Fig. 5i, several isolators are distributed on the six-ring labyrinth, which makes sure the inputting flexural waves are regulated to propagate along a pre-defined winding path and

reach the output finally. To demonstrate the unidirectional robustness of the linear passive circulator, we introduce different kinds of defects to the system. We deleted several unit cells, exchanged the locations of two unit cells and made different-shape defects to the waveguide in Fig. 5j–l, which corresponds to the defect types of ‘absence’, ‘disorder’ and ‘cavity’, respectively. The simulated normalized out-of-plane displacement fields at 12 kHz show that the defected circulator still have the stable performance in routing flexural waves propagation only along clockwise direction, almost no distortions or energy reduction. Therefore, the elastic circulator possesses remarkable superiority in customizability, versatile, anti-interference, which may potentially bring it into practical scenarios like energy harvesting, information processing, vibration isolation, etc.

We have reported and experimentally demonstrated a broadband and compact circulator platform for one-way elastic wave routing. By tailoring the wave vectors along waveguide, the perfect mode transition and energy trapping are achieved at the abrupt and continuous interfaces, respectively. Neither requiring the activated media, nor relying on nonlinear medium to break reciprocity, the circulator enables artful wave-vector modulation by passive and linear structures, upon which one-way transmission among three ports can be observed. Furthermore, based on the symmetry rules, the four-port versions are developed into different modes which enable steering waves forward port by port. As the offspring of circulator, a compact isolator is proposed for the isolation and trapping, which is also used to guide waves along the predefined path in a labyrinth. The circulator and its derivative are demonstrated having excellent performance including compact footprint, broadband effects, customized functions and robust ability. The circulator as beam splitter, combined with linear and passive strategies, provided a prosperous platform for on-chip integration at microwave frequencies<sup>42</sup>. It could pave the way for multiplexed signal routing and filtering. In addition, the highly efficient logic device gives rise to the possibility serving as signal-processing unit in mechanical and other digital wave circuits<sup>49</sup>. Furthermore, directionality arising from mode transition and mode trapping in the device has the important applications for the future directional devices, like unidirectional amplifiers and sensors<sup>50,51</sup>. The proposed prototype in this work also can be extended to other fields, like electromagnetic and acoustic waves. We can appreciate the potential application perspectives, including vibration and noise control, particle manipulating, energy harvesting, rectification and circulation.

## Methods

### Theory and simulation

The analytical dispersion relations of unit cells in Fig. 2a are obtained by calculating the flexural wave equations with continuous conditions. The detailed derivation is introduced in Supplementary Note 1. The numerical results are calculated by implementing Bloch condition for the unit cell and sweeping the wave vectors by finite element solver COMSOL Multiphysics. The perfectly matched layers (PML) are applied to both ends of parallel-plate waveguides to eliminate the effects of boundary reflections.

### Sample fabrication

The experimental circulator sample is fabricated by wire electrical-discharge machining in a steel plate with thickness  $\tau = 1.5$  mm. The material properties include Young's modulus  $E = 200$  GPa, density  $\rho = 7930$  kg·m<sup>-3</sup>, Poisson's rate  $\nu = 0.3$ . The lengths of cantilever beam  $l$  for each unit cell are listed in Supplementary Table S1.

### Experimental setup

The asymmetric manipulation functionalities of circulators are validated by using the Doppler laser vibration measurement system to observe the propagation of flexural waves intuitively. As shown in Supplementary Fig. S8, the experimental platform mainly consists of

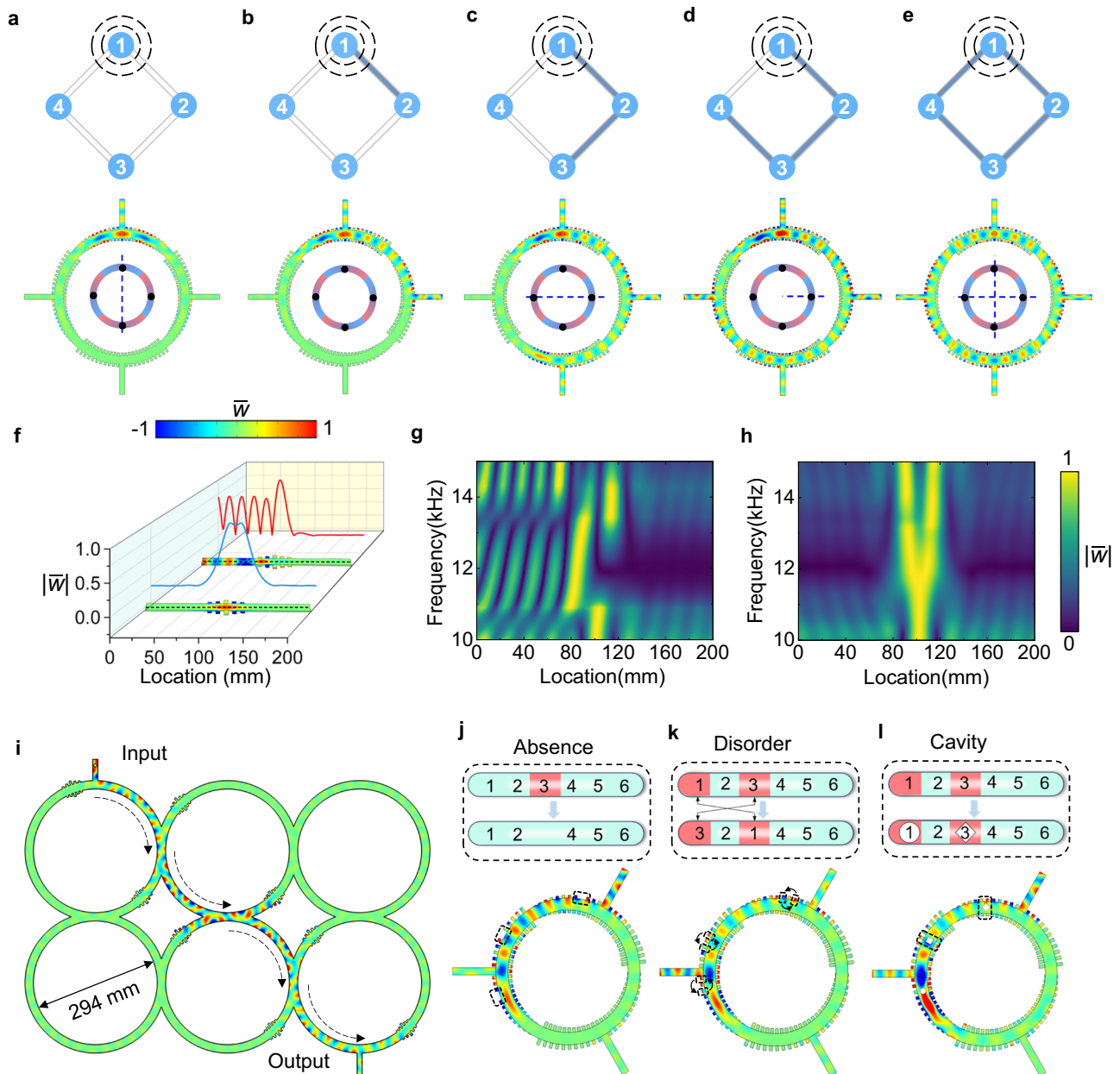


**Fig. 5 | Customized circulator, compact isolator and robustness demonstration.** **a–e** The exquisitely customized design of four-port circulators based on symmetry rules, which steer inputting waves propagate along the clockwise direction port by port. The gradient-color rings represent the configurations of different circulators. **f** The compact isolators to reflect and confine waves from the external and internal excitation sources. The normalized out-of-plane displacement

field  $\bar{w}$  and amplitude distribution  $|\bar{w}|$  along the black dashed line are displayed numerically. **g, h** The normalized amplitude  $|\bar{w}|$  versus location and frequency. The sources are placed at the left side and inside of the isolators, respectively. **i** Routing tailoring by several isolators in a six-ring labyrinth. The anti-interference demonstration of unidirectional robustness to different kinds of defects including (**j**) absence, (**k**) disorder and (**l**) cavity.

three parts: vibrometer, robot and controller, which are integrated for testing, moving and controlling, respectively. The excitation signal, a 10-cycle tune burst denoted as  $F(t) = [1 - \cos(\frac{2\pi f_c t}{10})] \sin(2\pi f_c t)$  with central frequency  $f_c = 12$  kHz, is generated by a signal generator (RIGOL DG4062). The signal is amplified by a power amplifier (ATA-2022H) and then transferred to a circular PZT which is bonded on the panel. At the same time, the controller is triggered to store the original and response signals. A Polytec Laser vibrometer (VFX-1-110) is used to capture the out-of-plane velocity by laser beam point by point. The scanning head is fixed on a 6-axis robotic arm, which enables free movement in space with high accuracy. The circulator is suspended on a metal frame by transparent wires. The captured signal is recorded

by an oscilloscope (PicoScope 4000 Series) and returned to controller. Once it is finished, the controller will automatically move the robot arm to the next point and the same procedure is repeated afterwards. The fast Fourier transform is carried out to convert the acquired data from time domain to frequency domain. The full field distributions at different frequencies and the transient animations of displacement amplitude are exported finally.

### Data availability

All data supporting the findings of this study are available within the article and its supplementary files. Source data are provided with this paper.



## Code availability

All technical details for producing the figures are enclosed in the manuscript and the Supplementary Information. Data are available from the corresponding authors upon request.

## References

- Feng, L. et al. Nonreciprocal light propagation in a silicon photonic circuit. *Science* **333**, 729–733 (2011).
- Mahmoud, A. M., Davoyan, A. R. & Engheta, N. All-passive non-reciprocal metastructure. *Nat. Commun.* **6**, 8359 (2015).
- Sounas, D. L. & Alù, A. Non-reciprocal photonics based on time modulation. *Nat. Photonics* **11**, 774–783 (2017).
- Tokura, Y. & Nagaosa, N. Nonreciprocal responses from non-centrosymmetric quantum materials. *Nat. Commun.* **9**, 3740 (2018).
- Nassar, H. et al. Nonreciprocity in acoustic and elastic materials. *Nat. Rev. Mater.* **5**, 667–685 (2020).
- Liang, B., Guo, X., Tu, J., Zhang, D. & Cheng, J. An acoustic rectifier. *Nat. Mater.* **9**, 989–992 (2010).
- Liang, B., Yuan, B. & Cheng, J.-c Acoustic diode: Rectification of acoustic energy flux in one-dimensional systems. *Phys. Rev. Lett.* **103**, 104301 (2009).
- Lepri, S. & Casati, G. Asymmetric wave propagation in nonlinear systems. *Phys. Rev. Lett.* **106**, 164101 (2011).
- Coulais, C., Sounas, D. & Alu, A. Static non-reciprocity in mechanical metamaterials. *Nature* **542**, 461–464 (2017).
- Popa, B.-I. & Cummer, S. A. Non-reciprocal and highly nonlinear active acoustic metamaterials. *Nat. Commun.* **5**, 3398 (2014).
- Trainiti, G. & Ruzzene, M. Non-reciprocal elastic wave propagation in spatiotemporal periodic structures. *New. J. Phys.* **18**, 083047 (2016).
- Merkel, A., Willatzen, M. & Christensen, J. Dynamic nonreciprocity in loss-compensated piezophononic media. *Phys. Rev. Appl.* **9**, 034033 (2018).
- Wang, Y. et al. Observation of nonreciprocal wave propagation in a dynamic phononic lattice. *Phys. Rev. Lett.* **121**, 194301 (2018).
- Karličič, D. et al. Non-reciprocal wave propagation in time-modulated elastic lattices with inerters. *Appl. Math. Model.* **117**, 316–335 (2023).
- Torrent, D., Poncelet, O. & Batsale, J.-C. Nonreciprocal thermal material by spatiotemporal modulation. *Phys. Rev. Lett.* **120**, 125501 (2018).
- Boechler, N., Theocharis, G. & Daraio, C. Bifurcation-based acoustic switching and rectification. *Nat. Mater.* **10**, 665–668 (2011).
- Shi, Y., Yu, Z. & Fan, S. Limitations of nonlinear optical isolators due to dynamic reciprocity. *Nat. Photonics* **9**, 388–392 (2015).
- Sounas, D. L. & Alù, A. Fundamental bounds on the operation of Fano nonlinear isolators. *Phys. Rev. B* **97**, 115431 (2018).
- Wang, Y.-T., Luan, P.-G. & Zhang, S. Coriolis force induced topological order for classical mechanical vibrations. *New. J. Phys.* **17**, 073031 (2015).
- Fleury, R., Sounas, D. L., Sieck, C. F., Haberman, M. R. & Alù, A. Sound isolation and giant linear nonreciprocity in a compact acoustic circulator. *Science* **343**, 516–519 (2014).
- Wang, Q. et al. Acoustic topological beam nonreciprocity via the rotational Doppler effect. *Sci. Adv.* **8**, eabq4451 (2022).
- Khanikaev, A. B., Fleury, R., Mousavi, S. H. & Alu, A. Topologically robust sound propagation in an angular-momentum-biased graphene-like resonator lattice. *Nat. Commun.* **6**, 8260 (2015).
- Ding, Y. et al. Experimental demonstration of acoustic Chern insulators. *Phys. Rev. Lett.* **122**, 014302 (2019).
- Schiff, L. & Snyder, H. Theory of the quadratic Zeeman effect. *Phys. Rev. B* **55**, 59 (1997).
- Xu, Y. et al. Broadband asymmetric waveguiding of light without polarization limitations. *Nat. Commun.* **4**, 2561 (2013).
- Cao, W.-K. et al. Asymmetric transmission of acoustic waves in a waveguide via gradient index metamaterials. *Sci. Bull.* **64**, 808–813 (2019).
- Long, Y. et al. Realization of acoustic spin transport in metasurface waveguides. *Nat. Commun.* **11**, 4716 (2020).
- Zhang, X., Zangeneh-Nejad, F., Chen, Z.-G., Lu, M.-H. & Christensen, J. A second wave of topological phenomena in photonics and acoustics. *Nature* **618**, 687–697 (2023).
- Xue, H., Yang, Y. & Zhang, B. Topological acoustics. *Nat. Rev. Mater.* **7**, 974–990 (2022).
- Ni, X., Yves, S., Krasnok, A. & Alu, A. Topological metamaterials. *Chem. Rev.* **123**, 7585–7654 (2023).
- Li, Y. et al. Tunable asymmetric transmission via lossy acoustic metasurfaces. *Phys. Rev. Lett.* **119**, 035501 (2017).
- Li, B. et al. Efficient asymmetric transmission of elastic waves in thin plates with lossless metasurfaces. *Phys. Rev. Appl.* **14**, 054029 (2020).
- Su, G., Du, Z., Jiang, P. & Liu, Y. High-efficiency wavefront manipulation in thin plates using elastic metasurfaces beyond the generalized Snell's law. *Mech. Syst. Signal. Pr.* **179**, 109391 (2022).
- Hu, Y. et al. Realization of ultrathin waveguides by elastic gratings. *Commun. Phys.* **5**, 62 (2022).
- Wang, X., Fang, X., Mao, D., Jing, Y. & Li, Y. Extremely asymmetrical acoustic metasurface mirror at the exceptional point. *Phys. Rev. Lett.* **123**, 214302 (2019).
- Li, X., Yu, Z., Iizuka, H. & Lee, T. Experimental demonstration of extremely asymmetric flexural wave absorption at the exceptional point. *Extrem. Mech. Lett.* **52**, 101649 (2022).
- Doppler, J. et al. Dynamically encircling an exceptional point for asymmetric mode switching. *Nature* **537**, 76–79 (2016).
- Long, Y., Ren, J. & Chen, H. Intrinsic spin of elastic waves. *Proc. Natl. Acad. Sci. USA* **115**, 9951–9955 (2018).
- Liu, Y. et al. Willis metamaterial on a structured beam. *Phys. Rev. X* **9**, 011040 (2019).
- Zanotto, S., Biasiol, G., Santos, P. V. & Pitanti, A. Metamaterial-enabled asymmetric negative refraction of GHz mechanical waves. *Nat. Commun.* **13**, 5939 (2022).
- Ma, J., Zhou, D., Sun, K., Mao, X. & Gonella, S. Edge modes and asymmetric wave transport in topological lattices: Experimental characterization at finite frequencies. *Phys. Rev. Lett.* **121**, 094301 (2018).
- Barzanjeh, S. et al. Mechanical on-chip microwave circulator. *Nat. Commun.* **8**, 953 (2017).
- Ju, R. et al. Nonreciprocal heat circulation metadevices. *Adv. Mater.* **36**, 2309835 (2024).
- Tsakmakidis, K. L. et al. Breaking Lorentz reciprocity to overcome the time-bandwidth limit in physics and engineering. *Science* **356**, 1260–1264 (2017).
- Li, J. et al. Single-photon circulator by spinning optical resonators. *Opt. Express* **32**, 35781–35793 (2024).
- Peng, B. et al. Chiral modes and directional lasing at exceptional points. *Proc. Natl. Acad. Sci. USA* **113**, 6845–6850 (2016).
- Shu, F.-J., Zou, C.-L., Zou, X.-B. & Yang, L. Chiral symmetry breaking in a microring optical cavity by engineered dissipation. *Phys. Rev. A* **94**, 013848 (2016).
- Chen, H.-Z. et al. Revealing the missing dimension at an exceptional point. *Nat. Phys.* **16**, 571–578 (2020).
- Szulc, K., Graczyk, P., Mruczkiewicz, M., Gubbiotti, G. & Krawczyk, M. Spin-wave diode and circulator based on unidirectional coupling. *Phys. Rev. Appl.* **14**, 034063 (2020).
- Sliwa, K. et al. Reconfigurable Josephson circulator/directional amplifier. *Phys. Rev. X* **5**, 041020 (2015).
- Beli, D., Silva, P. B. & de França Arruda, J. R. Mechanical circulator for elastic waves by using the nonreciprocity of flexible rotating rings. *Mech. Syst. Signal. Pr.* **98**, 1077–1096 (2018).

## Acknowledgements

This work is supported by the National Natural Science Foundation of China (NSFC) under Grant Nos. 12272298 and 12172271. J. C. acknowledges support from the Spanish Ministry of Science under grant PID2023-150075OB-I00. Y. H. acknowledges support from the China Scholarship Council (CSC) through Grant No. 202306290133.

## Author contributions

J.C., B. L. and Y. Liu supervised the project. B. L. and Y. H. conceived the original idea. Y. H., Y. Liu and B. L. performed the theoretical calculation and numerical simulation. Y. H. and Y. Li carried out the experiments and analyzed the data. J.C., B. L. and Y. Liu helped with the theoretical interpretation. Y. H., B. L., Y. Liu and J.C. wrote the manuscript. All authors contributed to scientific discussions and modifications of the manuscript.

## Competing interests

The authors declare no competing interests.

## Additional information

**Supplementary information** The online version contains supplementary material available at <https://doi.org/10.1038/s41467-025-59313-0>.

**Correspondence** and requests for materials should be addressed to Yongquan Liu, Bing Li or Johan Christensen.

**Peer review information** *Nature Communications* thanks Zhongming Gu, and the other, anonymous, reviewer(s) for their contribution to the peer review of this work. A peer review file is available.

**Reprints and permissions information** is available at <http://www.nature.com/reprints>

**Publisher's note** Springer Nature remains neutral with regard to jurisdictional claims in published maps and institutional affiliations.

**Open Access** This article is licensed under a Creative Commons Attribution-NonCommercial-NoDerivatives 4.0 International License, which permits any non-commercial use, sharing, distribution and reproduction in any medium or format, as long as you give appropriate credit to the original author(s) and the source, provide a link to the Creative Commons licence, and indicate if you modified the licensed material. You do not have permission under this licence to share adapted material derived from this article or parts of it. The images or other third party material in this article are included in the article's Creative Commons licence, unless indicated otherwise in a credit line to the material. If material is not included in the article's Creative Commons licence and your intended use is not permitted by statutory regulation or exceeds the permitted use, you will need to obtain permission directly from the copyright holder. To view a copy of this licence, visit <http://creativecommons.org/licenses/by-nc-nd/4.0/>.

© The Author(s) 2025